

Connecting Topological Anderson and Mott Insulators in Disordered Interacting Fermionic Systems

Guo-Qing Zhang,^{1,2} Ling-Zhi Tang,¹ Ling-Feng Zhang,¹ Dan-Wei Zhang,^{1,2,*} and Shi-Liang Zhu^{1,2}

¹Guangdong Provincial Key Laboratory of Quantum Engineering and Quantum Materials,
School of Physics and Telecommunication Engineering,

South China Normal University, Guangzhou 510006, China

²Guangdong-Hong Kong Joint Laboratory of Quantum Matter,

Frontier Research Institute for Physics, South China Normal University, Guangzhou 510006, China

(Dated: June 2, 2022)

The topological Anderson and Mott insulators are two different phases beyond topological band insulators, and have so far been separately widely explored. Here we combine them into a single system of spin-1/2 interacting fermionic atoms in a disordered optical lattice. We find that the topological Anderson and Mott insulators in the noninteracting and clean limits can be adiabatically connected without gap closing in the phase diagram of our model. Lying between the two phases, we uncover a disordered correlated topological insulator, which is induced from a trivial band insulator by the combination of disorder and interaction, as the generalization of topological Anderson insulators to the many-body interacting regime. The phase diagram is determined by numerically calculating various topological properties and confirmed by unsupervised and automated machine learning. We develop a unified approach to reveal topological phase transitions driven from interaction and disorder renormalized Zeeman terms. The topological phases can be detected from disorder/interaction induced topological edge excitations and charge pumping in optical lattices.

Introduction.—Topological insulators with intriguing properties that are robust against certain disorder and correlations have been well understood in the framework of topological band theory under the independent particle approximation [1–3]. For strong disorder, the energy bands generally become trivial due to the Anderson localization of Bloch states [4]. Strikingly, it was found that a topological phase can be induced from a trivial phase by disorders, known as topological Anderson insulator (TAI) [5]. The TAIs have been theoretically studied [5–20] and experimentally observed in various system, such as cold atomic lattices [21], photonic and sonic crystals [22–24], and electric circuits [25]. The studies of TAIs up to now are all focused on the single-particle level without inter-particle interactions.

Topological bands are stable with respect to weak or moderate interactions [26]. Remarkably, interactions can induce exotic correlated topological phases [27], such as fractional quantum Hall effects [28] and topological Mott insulator (TMI) [29]. It has been shown that TMIs are a generic class of interaction-induced topological phases for interacting fermions or bosons [29–46], characterized by many-body topological invariants for Mott ground states and edge excitations, and realizable with ultracold atoms in optical lattices [37–44]. The interaction-induced TMIs and disorder-induced TAIs are well-known as two distinct topological phases and separately explored so far. It remains unclear whether the two topological phases can exhibit in a single system. If yes, how can they be connected and what are the phases lying between them? Can the TAIs exhibit in the presence of interactions?

In this Letter, we address these important questions by exploring topology of spin-1/2 interacting fermions in a

disordered 1D optical lattice (OL). Our main results are: (i) We combine the TAI and TMI in the noninteracting and clean limits into this system and find that they can be adiabatically connected without gap closing. (ii) Lying between them, we uncover a disordered correlated topological insulator (DCTI) induced by the combination of disorder and interaction from a trivial band insulator (BI), as the first generalization of noninteracting TAIs to the many-body interacting regime. (iii) We not only numerically calculate various topological characteristics and use unsupervised and automated machine learning to determine the phase diagram, but also develop an analytical approach to reveal topological phase transitions driven by interaction/disorder renormalized Zeeman terms with the mean-field (MF) and self-consistent Born approximations (SCBAs). Moreover, the revealed topological phases can be detected from the interaction/disorder induced topological edge excitations and charge pumping in OLs. Our work paves the way to search on exotic topological phases in disordered interacting systems.

Model and phase diagram.—We consider an atomic gas of spin-1/2 interacting fermions in a 1D spin-dependent OL with disordered ladder potentials [47–52], as shown in Fig. 1(a). The tight-binding Hamiltonian reads

$$\begin{aligned} H = & -t \sum_j (c_{j\uparrow}^\dagger c_{j+1\uparrow} - c_{j\downarrow}^\dagger c_{j+1\downarrow} + \text{H.c.}) \\ & + t_s \sum_j (c_{j\uparrow}^\dagger c_{j+1\downarrow} - c_{j\downarrow}^\dagger c_{j+1\uparrow} + \text{H.c.}) \\ & + \sum_j m_j (n_{j\uparrow} - n_{j\downarrow}) + U \sum_{j\sigma=\uparrow,\downarrow} n_{j\sigma} n_{j+1\sigma}, \end{aligned} \quad (1)$$

where $n_{j\sigma} = c_{j\sigma}^\dagger c_{j\sigma}$ and $c_{j\sigma}^\dagger$ ($c_{j\sigma}$) creates (annihilates) a

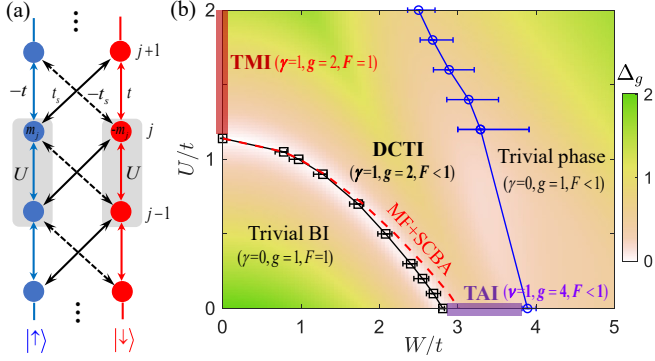


FIG. 1. (Color online) (a) Proposed model for interacting fermions in a spin-dependent optical ladder with disordered potentials. (b) Phase diagram of the Hamiltonian (1) on the $W-U$ plane. The square and circle symbols guided by the solid lines are obtained from topological invariants γ and ν , and the error bars denotes the uncertainty due to disorder. The two colored thick lines correspond to the TMI and TAI phases in the clean and noninteracting limits, which are connected via the DCTI phase and become a disordered trivial phase for stronger disorders. The red dashed line denotes the topological phase boundary between the trivial BI and the topological phases, determined using the MF and SCBA approaches. The excitation gap Δ_g is plotted as the background. Parameters are $t = 1$, $t_s = 0.95$, $m_z = 3$, and $\alpha = (\sqrt{5} - 1)/2$.

spin- σ fermion ($\sigma = \uparrow, \downarrow$) at site j ($j = 1, 2, \dots, L$) of the two-leg ladder of length L . Here t (t_s) denotes the spin-conserved (spin-flip) hopping and $t \equiv 1$ as the energy unit, m_j is the disordered potential acting as an effective random Zeeman field, and U is the density-density interaction strength between fermions residing in neighboring sites along each leg of the ladder. We focus on the half-filling case with total atomic number $N_a = L$ and the quasiperiodic disorder $m_j = m_z + W \cos(2\pi\alpha j + \varphi)$ with m_z the overall Zeeman strength, W the disorder strength, $\alpha = (\sqrt{5} - 1)/2$ an irrational number, and φ an offset phase randomly chosen for sampling. In experiments, two hyperfine states of fermionic atoms can be used to construct the spin-1/2 system. The spin-dependent optical ladder lattice can be realized using proper laser beams with incommensurate potential acting on the two states with opposite detunings [48–52]. The spin-flip and spin-dependent hopping terms can be engineered by Raman-assisted tunnelings in OLs [53–60].

The model has a topological insulator for $|m_z| < 2t$ in the $U = W = 0$ limit, which is characterized by the 1D winding number ν and protected by the chiral symmetry in the AIII class [53]. The disorder and interaction considered here preserve the chiral symmetry. We study the many-body ground state of the Hamiltonian (1) by using the exact diagonalization (ED) and density-matrix renormalization group (DMRG) methods [61–63], the unsupervised and automated machine learning [64–67], and the MF and SCBA approaches [6–8]. The quantities are

averaged over 20 quasiperiodic configurations in numerical simulations. The random disorder case with similar results is given in the Supplemental Material (SM) [68].

Our main results are summarized in the ground-state phase diagram on the $W-U$ plane [see Fig. 1(b)]. The ordered and disordered phases against disorders are described by the unity and non-unity fidelity (F), respectively. The topological phases are characterized by the topological invariants (winding number ν or quantized Berry phase γ) and ground-state degeneracy g under open boundary condition (OBC). For small W and U , the ground state is an ordered trivial BI. In the clean (noninteracting) limit $W = 0$ ($U = 0$), the ground state becomes an ordered TMI (single-particle TAI) with increasing U (W) up to the topological phase transition point $U_c \approx 1.14$ ($W_c \approx 2.8$). For finite U and W , a DCTI phase exhibits and preserves the topological character of TMIs with disordered ground states. Strikingly, the DCTI can be driven from the trivial BI with increasing W for $U \lesssim 1.14$ with a topological phase transition. Such a topological phase induced by the combination of moderate disorder and interaction broadens the concept of TAIs to the many-body interacting regime. The first phase boundary between the trivial BI and the topological phases indicated by the square symbols and guided by the black solid line are obtained by numerical calculations of the topological invariants and some complementary quantities, which agrees well with the one obtained analytically using the MF and SCBA approaches. For strong disorder, the DCTI and TAI become a disordered trivial phase with the second phase boundary denoted by the circle symbols and the blue solid line. The excitation gap $\Delta_g = E_1 - E_0$ between the ground state with energy E_0 and the first excited state with energy E_1 under periodic boundary condition (PBC) is plotted as the background of Fig. 1(b). We find the bulk gap closing (unclosing) in the first (second) topological phase boundary. Moreover, the TAI and TMI are adiabatically connected via the DCTI without gap closing in the phase diagram. Below we elaborate these topological phases.

Before proceeding, we make some remarks on the phase diagram. First, the finite-size scalings of topological invariants and bulk gap are used to confirm the topological phases and their adiabatic connections, based on the DMRG for the system up to $L = N_a = 48$ [68]. Second, the DCTI and TMI belong to the symmetry-protected topological phases of interacting fermions with a symmetry group $U(1) \times Z_2^T$ [69–71], whose ground states at half filling under OBC are twofold degenerate ($g = 2$) with one topological edge excitation occupied on each edge. In contrast, the ground state for the noninteracting TAIs (trivial phases) is fourfold (non-degenerate) degenerate ($g = 4$) as two zero-energy edge modes can be either empty or occupied. We numerically confirm the ground-state degeneracy for different phases [68]. Third, we use the machine learning approach in a unsupervised and au-

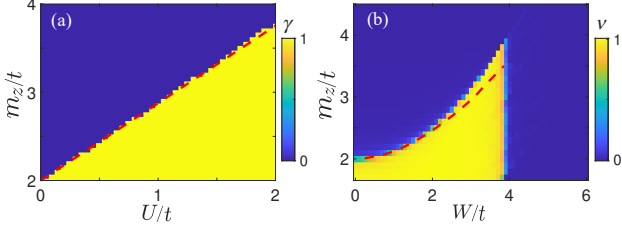


FIG. 2. (Color online) (a) Quantized Berry phase γ as a function of U and m_z for $W = 0$ and $L = 8$. (b) Winding number ν as a function of W and m_z for $U = 0$ and $L = 610$. The red dashed lines correspond to the phase boundaries determined using the MF and SCBA approximations. Other parameters are the same to those in Fig. 1.

tomated fashion [64–66] to confirm the phase diagram with the well matched phase boundaries [68]. Finally, the DCTI driven by disorder and interaction can preserve while the TAI is absent for certain values of m_z [68].

TMI and TAI in two limits.— The topological properties of the many-body ground states can be characterized by a quantized Berry phase in unit of π under twisted boundary condition [26, 49]: $\gamma = \frac{i}{\pi} \oint \langle \psi^g(\theta) | \frac{d}{d\theta} | \psi^g(\theta) \rangle$ with mod 2, where $|\psi^g(\theta)\rangle$ is the ground state wave function with the twist boundary phase θ [72]. Here $\gamma = 1$ and 0 for topological and trivial phases, respectively. In the clean limit $W = 0$, we calculate γ and obtain the topological phase diagram on the U - m_z plane, as shown in Fig. 2(a). The ground state lies at the trivial BI phase for $m_z/t > 2$ and $U = 0$, and becomes a TMI with increasing U up to the critical interaction U_c . We find that U_c linearly depends on m_z and $U_c \approx 1.14$ for $m_z = 3$. We also calculate Δ_g to confirm the topological phase transition accompanied with gap closing and reopening.

In the $U = 0$ limit, the quantized Berry phase corresponds to the winding number for this 1D chiral system [59]. In the presence of disorder, the winding number ν can be numerically calculated with real-space Hamiltonian and averaged over disorder samples [11]. The result of ν on the W - m_z plane is shown in Fig. 2(b), which reveals the disorder-induced TAI phase when $2 \lesssim m_z \lesssim 3.8$. For $m_z = 3$ in Fig. 1(b), we obtain the TAI for disorder strength $2.8 \lesssim W \lesssim 3.9$. Note that the single-particle energy gap also closes at the topological phase transition from the trivial BI to the TAI.

DCTI and topological phase transitions.— For finite interaction and disorder, we calculate the Berry phase γ of the many-body ground state as a function of W and U in Fig. 3(a) for $m_z = 3$, which indicates three regimes for topologically trivial and nontrivial phases. We confirm our results by gap and entanglement calculations. The half-chain entanglement \mathcal{S} is defined as the von Neumann entropy [73]: $\mathcal{S} = -\text{Tr}_B[\rho_A \ln \rho_A]$ with $\rho_A = \text{Tr}_B|\psi^g\rangle\langle\psi^g|$ being the reduced density matrix of two halves labeled by

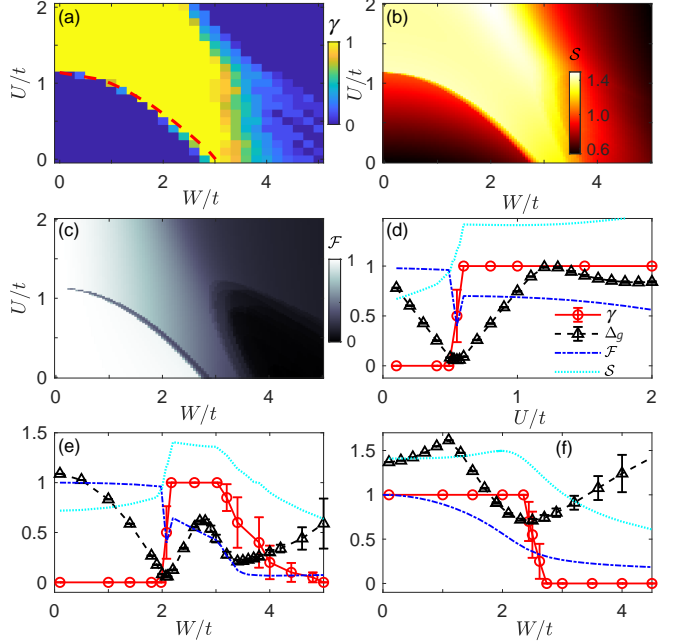


FIG. 3. (Color online) (a) Quantized Berry phase γ , (b) half-chain entanglement \mathcal{S} , and (c) ground-state fidelity \mathcal{F} as functions of W and U . The red dashed line in (a) is the phase boundary determined using the MF and SCBA approximations. (d-f) The quantities γ , Δ_g , \mathcal{F} and \mathcal{S} as functions of U or W for $W = 2$ (d), $U = 0.5$ (e), and $U = 2$ (f), respectively. Other parameters are the same to those in Fig. 1.

A and B. As shown in Fig. 3(b), the large \mathcal{S} indicates the topological phase that is highly entangled and consists with the result in Fig. 3(a). We also calculate the fidelity \mathcal{F} of the ground state wave function against disorder, which is defined as $\mathcal{F} = \frac{2}{N_d(N_d-1)} \sum_{i \neq j} \langle \psi^g(\varphi_i) | \psi^g(\varphi_j) \rangle$, with $\varphi_{i,j}$ the random phases chosen from N_d disorder samples. As shown in Fig. 3(c), the fidelity \mathcal{F} keeps nearly 1 in the ordered phase, which is well separated from the disordered phase with $\mathcal{F} < 1$.

From these numerical results and previous discussions, we can find three distinct phases under disorder and interaction: the ordered trivial BI for small U and W connecting to the $U = W = 0$ limit, the DCTI connecting the TAI and TMI as a generalization of single-particle TAI to many-body interacting regime, and the disordered trivial phase for large W . There are three typical topological phase transitions with increasing U or W , as shown in Figs. 3(d-f). For the first case with increasing U and fixed $W = 2$ in Fig. 3(d), the topological invariant changes from $\gamma = 0$ to 1 with the excitation gap closing ($\Delta_g \approx 0$) at the critical interaction strength. Near the critical point, the fidelity \mathcal{F} decreases sharply from unity and the entanglement \mathcal{S} increases quickly. These results signal the topological phase transition from an ordered trivial BI to the DCTI. For the second case with increasing W and fixed $U = 0.5$ in Fig. 3(e), the disorder-

induced topological phase transition from the BI to the DCTI is also indicated by the change of the topological invariant and other quantities. However, with further increasing W , the DCTI becomes a disordered trivial phase without gap closing, where γ is not well quantized due to the disorder fluctuation and finite size effect. For the third case with increasing W and fixed $U = 2$ in Fig. 3(f), the topological phase transition from the DCTI to the trivial phase is well indicated by the sharp change of the values of γ , \mathcal{F} and \mathcal{S} , but without gap closing. By repeating the procedure of determining the transition points at different values of U and W , which are labeled by the square and circle symbols in Fig. 1(b), we map out the phase diagram. We also find that the phase boundary with the square symbols is accompanied by the discontinuity of the total magnetization [68].

Unified analysis of phase boundaries.—Based on the MF and SCBA mehtods, we develop a unified approach to obtain the phase boundaries between the trivial BI and different topological phases. Under the Hartree-Fock MF approximation, the density-density interaction term in Hamiltonian (1) can be linearized as $n_{j\sigma}n_{j+1\sigma} \approx \langle n_{j\sigma} \rangle n_{j+1\sigma} + \langle n_{j+1\sigma} \rangle n_{j\sigma} - \langle n_{j\sigma} \rangle \langle n_{j+1\sigma} \rangle$. We find that the interaction term in the BI phase can be further simplified to $\sum_{j\sigma} n_{j\sigma}n_{j+1\sigma} \approx \rho_s U \sum_j (n_{j\uparrow} - n_{j\downarrow})$ up to an irrelevant constant with ρ_s being the spin density difference (the spin density distribution of the ground state is nearly site-independent) [68]. Thus, the interaction effectively renormalizes the Zeeman term. By numerically determining ρ_s , we obtain the interaction-renormalized Zeeman strength $\tilde{m}_z \approx m_z - U/1.14$ [68]. In the clean limit, the interaction-induced TMI emerges when $|\tilde{m}_z| < 2$, which agrees well with the topological phase boundary shown in Fig. 2(a). The analysis works in the ordered BI regime where the disorder is not dominated. The disorder effect can be accounted based on an effective medium theory and the SCBA method [6–8]. The key of the SCBA method is to self-consistently obtain the self-energy introduced by the disorder, and then to include the self-energy as renormalization to the clean Hamiltonian. For our model, the self-energy term $\Sigma(W)$ satisfies the self-consistent equation [68]

$$\frac{1}{E_f - H_{\text{MF}}(k) - \Sigma(W)} = \left\langle \frac{1}{E_f - H_{\text{eff}}(k, W_q)} \right\rangle_q, \quad (2)$$

where $E_f \equiv 0$ is the Fermi energy, $H_{\text{MF}}(k) = (\tilde{m}_z - 2t \cos k)\sigma_z - 2t_s \sin k \sigma_y$ with $\sigma_{y,z}$ the Pauli matrices is the clean MF Hamiltonian, H_{eff} denotes the effective Hamiltonian renormalized by the disorder $W_q = W \cos(2\pi\alpha q)$ with index $q = 1, 2, \dots, N_q$, and $\langle \dots \rangle_q$ denotes averaging over N_q disorder samples. Here the self-energy is given by $\Sigma = \Sigma_z \sigma_z + \Sigma_y \sigma_y$. After numerically obtaining $\Sigma(W)$ for given W [68], the Zeeman strength \tilde{m}_z and the hopping strength t_s are renormalized according to $\tilde{m}_z = \tilde{m}_z + \Sigma_z \approx m_z - U/1.14 + \Sigma_z$ and $\tilde{t}_s = t_s + \Sigma_y$. This produces the topological phase boundaries at $|\tilde{m}_z| = 2$,

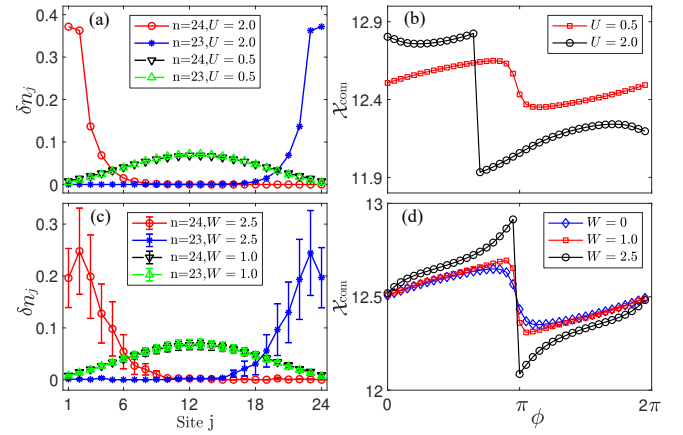


FIG. 4. (Color online) Quasiparticle density distribution δn_j and center-of-mass $\mathcal{X}_{\text{com}}(\phi)$ for $W = 0$ (a,b) and $U = 0.5$ (c,d) with $L = 24$. Other parameters are the same to those in Fig. 1.

which are plotted as the red dashed lines in Figs. 1–3 and agree well with the numerical results. Thus, the topological phase transitions from the trivial BI to topological phases can be attributed to the interaction and disorder renormalization on the Zeeman strength.

Proposed detections.—Finally, we propose that the correlated topological phases may be detected from the disorder/interaction induced topological edge excitations and charge pumping [74] in the OL. The appearance of in-gap boundary states is a hallmark of topological phases. In the presence of interactions, the edge states are collective modes instead of noninteracting fermions. The density distribution of the quasiparticle excitation when a fermion is added to the lattice filled by n fermions can be defined as $\delta n_j = \langle \psi_{n+1}^g | n_j | \psi_{n+1}^g \rangle - \langle \psi_n^g | n_j | \psi_n^g \rangle$ [26], where $|\psi_n^g\rangle$ is the ground state of filling n fermions under OBC, and $n_j = n_{j\uparrow} + n_{j\downarrow}$. By the DMRG simulation, we numerically calculate δn_j for $L = 24$ and $n = 23, 24$. As shown in Figs. 4(a) and 4(c), the interaction and disorder can induce edge excitations when the system is driven from the trivial BI to the TMI and correlated TAI, respectively. The topological edge modes can be measured from the atomic local density distribution [75].

The topological pumping allows a quantized particle transport when adiabatically encircling in parameter space [74, 76]. We design a pump scheme by tuning the parameters in Hamiltonian (1): $\pm t_s \rightarrow \pm t_s(1 + \sin \phi)$ and $m_z \rightarrow m_z + 0.5 \cos \phi$ via the phase ϕ varying from 0 to 2π . The charge pumping can be observed from the center of mass of the atomic gas in the OL with respect to the adiabatic parameter [77–82], which is given by $\mathcal{X}_{\text{com}}(\phi) = \frac{1}{N_d} \sum_j j \langle \psi^g(\phi) | n_j | \psi^g(\phi) \rangle$ under OBC. As shown in Figs. 4(b) and 4(d), when the system is driven from the BI to the TMI or correlated TAI, the center of mass $\mathcal{X}_{\text{com}}(\phi)$ shows a nearly one-unit-cell jump as the quantized charge pumping. Our results indicate that the

bulk-boundary correspondence, which involves the topological invariants/charge pumping and edge states, holds for the disorder/interaction induced topological phases.

Conclusion.—In summary, we have demonstrated that the TAI and TMI phases can emerge and adiabatically connected without gap closing in a single system of spin-1/2 interacting fermions in a 1D disordered OL. We have uncovered a correlated TAI phase induced by the combination of disorder and interaction, providing the first generalization of TAI to the many-body interacting regime. We have developed a unified theory to obtain the phase boundaries between the trivial BI and different topological phases. The predicted topological phases could be detected from the disorder/interaction induced topological edge excitations and charge pumping in OLs.

Note added: Recently, we noticed a related work on the symmetry-protected topological phase of hard-core bosons in 1D Rydberg atom chains with structural disorders [83].

This work was supported by the National Natural Science Foundation of China (Grants No. U1830111, No. 12047522, No. 12074180, and No. U1801661), the Key-Area Research and Development Program of Guangdong Province (Grant No. 2019B030330001), the Science and Technology of Guangzhou (Grants No. 2019050001), and the Guangdong Basic and Applied Basic Research Foundation (Grants No. 2020A1515110290 and No. 2021A1515010315).

* danweizhang@m.scnu.edu.cn

- [1] M. Z. Hasan and C. L. Kane, *Rev. Mod. Phys.* **82**, 3045 (2010).
- [2] X.-L. Qi and S.-C. Zhang, *Rev. Mod. Phys.* **83**, 1057 (2011).
- [3] A. Bansil, H. Lin, and T. Das, *Rev. Mod. Phys.* **88**, 021004 (2016).
- [4] P. W. Anderson, *Phys. Rev.* **109**, 1492 (1958).
- [5] J. Li, R.-L. Chu, J. K. Jain, and S.-Q. Shen, *Phys. Rev. Lett.* **102**, 136806 (2009).
- [6] C. W. Groth, M. Wimmer, A. R. Akhmerov, J. Tworzydlo, and C. W. J. Beenakker, *Phys. Rev. Lett.* **103**, 196805 (2009).
- [7] H. Jiang, L. Wang, Q.-F. Sun, and X. C. Xie, *Phys. Rev. B* **80**, 165316 (2009).
- [8] C.-Z. Chen, J. Song, H. Jiang, Q.-f. Sun, Z. Wang, and X. C. Xie, *Phys. Rev. Lett.* **115**, 246603 (2015).
- [9] H.-M. Guo, G. Rosenberg, G. Refael, and M. Franz, *Phys. Rev. Lett.* **105**, 216601 (2010).
- [10] A. Altland, D. Bagrets, L. Fritz, A. Kamenev, and H. Schmiedt, *Phys. Rev. Lett.* **112**, 206602 (2014).
- [11] I. Mondragon-Shem, T. L. Hughes, J. Song, and E. Prodan, *Phys. Rev. Lett.* **113**, 046802 (2014).
- [12] P. Titum, N. H. Lindner, M. C. Rechtsman, and G. Refael, *Phys. Rev. Lett.* **114**, 056801 (2015).
- [13] P. V. Sriluckshmy, K. Saha, and R. Moessner, *Phys. Rev. B* **97**, 024204 (2018).
- [14] R. Chen, D.-H. Xu, and B. Zhou, *Phys. Rev. B* **100**, 115311 (2019).
- [15] D.-W. Zhang, L.-Z. Tang, L.-J. Lang, H. Yan, and S.-L. Zhu, *Sci. China-Phys. Mech. Astron.* **63**, 267062 (2020).
- [16] X.-W. Luo and C. Zhang, *arXiv:1912.10652v1*.
- [17] H. Wu and J.-H. An, *Phys. Rev. B* **102**, 041119 (2020).
- [18] X. S. Wang, A. Brataas, and R. E. Troncoso, *Phys. Rev. Lett.* **125**, 217202 (2020).
- [19] C.-A. Li, B. Fu, Z.-A. Hu, J. Li, and S.-Q. Shen, *Phys. Rev. Lett.* **125**, 166801 (2020).
- [20] Y.-B. Yang, K. Li, L.-M. Duan, and Y. Xu, *Phys. Rev. B* **103**, 085408 (2021).
- [21] E. J. Meier, F. A. An, A. Dauphin, M. Maffei, P. Massignan, T. L. Hughes, and B. Gadway, *Science* **362**, 929 (2018).
- [22] S. Stützer, Y. Plotnik, Y. Lumer, P. Titum, N. H. Lindner, M. Segev, M. C. Rechtsman, and A. Szameit, *Nature* **560**, 461 (2018).
- [23] G.-G. Liu, Y. Yang, X. Ren, H. Xue, X. Lin, Y.-H. Hu, H.-x. Sun, B. Peng, P. Zhou, Y. Chong, and B. Zhang, *Phys. Rev. Lett.* **125**, 133603 (2020).
- [24] F. Zangeneh-Nejad and R. Fleury, *Adv. Mater.* **32**, 2001034 (2020).
- [25] W. Zhang, D. Zou, Q. Pei, W. He, J. Bao, H. Sun, and X. Zhang, *Phys. Rev. Lett.* **126**, 146802 (2021).
- [26] H. Guo and S.-Q. Shen, *Phys. Rev. B* **84**, 195107 (2011).
- [27] S. Rachel, *Rep. Prog. Phys.* **81**, 116501 (2018).
- [28] D. C. Tsui, H. L. Stormer, and A. C. Gossard, *Phys. Rev. Lett.* **48**, 1559 (1982).
- [29] S. Raghu, X.-L. Qi, C. Honerkamp, and S.-C. Zhang, *Phys. Rev. Lett.* **100**, 156401 (2008).
- [30] Y. Zhang, Y. Ran, and A. Vishwanath, *Phys. Rev. B* **79**, 245331 (2009).
- [31] T. Yoshida, R. Peters, S. Fujimoto, and N. Kawakami, *Phys. Rev. Lett.* **112**, 196404 (2014).
- [32] I. F. Herbut and L. Janssen, *Phys. Rev. Lett.* **113**, 106401 (2014).
- [33] A. Amaricci, J. C. Budich, M. Capone, B. Trauzettel, and G. Sangiovanni, *Phys. Rev. Lett.* **114**, 185701 (2015).
- [34] J. Imriška, L. Wang, and M. Troyer, *Phys. Rev. B* **94**, 035109 (2016).
- [35] S. Barbarino, G. Sangiovanni, and J. C. Budich, *Phys. Rev. B* **99**, 075158 (2019).
- [36] B. Irsigler, J.-H. Zheng, and W. Hofstetter, *Phys. Rev. Lett.* **122**, 010406 (2019).
- [37] A. Dauphin, M. Müller, and M. A. Martin-Delgado, *Phys. Rev. A* **86**, 053618 (2012).
- [38] S.-L. Zhu, Z.-D. Wang, Y.-H. Chan, and L.-M. Duan, *Phys. Rev. Lett.* **110**, 075303 (2013).
- [39] X. Deng and L. Santos, *Phys. Rev. A* **89**, 033632 (2014).
- [40] Y. Kuno, K. Shimizu, and I. Ichinose, *New J. Phys.* **19**, 123025 (2017).
- [41] F. Grusdt, M. Höning, and M. Fleischhauer, *Phys. Rev. Lett.* **110**, 260405 (2013).
- [42] Z. Xu and S. Chen, *Phys. Rev. B* **88**, 045110 (2013).
- [43] H. Hu, S. Chen, T.-S. Zeng, and C. Zhang, *Phys. Rev. A* **100**, 023616 (2019).
- [44] Y.-L. Chen, G.-Q. Zhang, D.-W. Zhang, and S.-L. Zhu, *Phys. Rev. A* **101**, 013627 (2020).
- [45] D.-W. Zhang, Y.-L. Chen, G.-Q. Zhang, L.-J. Lang, Z. Li, and S.-L. Zhu, *Phys. Rev. B* **101**, 235150 (2020).
- [46] Y.-X. Wang and D.-X. Qi, *Phys. Rev. B* **99**, 075204 (2019).
- [47] M. Creutz, *Phys. Rev. Lett.* **83**, 2636 (1999).

[48] M. Atala, M. Aidelsburger, M. Lohse, J. T. Barreiro, B. Paredes, and I. Bloch, *Nat. Phys.* **10**, 588 (2014).

[49] J. Jünemann, A. Piga, S.-J. Ran, M. Lewenstein, M. Rizzi, and A. Bermudez, *Phys. Rev. X* **7**, 031057 (2017).

[50] J. H. Kang, J. H. Han, and Y. Shin, *Phys. Rev. Lett.* **121**, 150403 (2018).

[51] G. Roati, C. D’Errico, L. Fallani, M. Fattori, C. Fort, M. Zaccanti, G. Modugno, M. Modugno, and M. Inguscio, *Nature* **453**, 895 (2008).

[52] M. Schreiber, S. S. Hodgman, P. Bordia, H. P. Lüschen, M. H. Fischer, R. Vosk, E. Altman, U. Schneider, and I. Bloch, *Science* **349**, 842 (2015).

[53] X.-J. Liu, K. T. Law, T. K. Ng, and P. A. Lee, *Phys. Rev. Lett.* **111**, 120402 (2013).

[54] X. Zhou, J.-S. Pan, Z.-X. Liu, W. Zhang, W. Yi, G. Chen, and S. Jia, *Phys. Rev. Lett.* **119**, 185701 (2017).

[55] Z. Wu, L. Zhang, W. Sun, X.-T. Xu, B.-Z. Wang, S.-C. Ji, Y. Deng, S. Chen, X.-J. Liu, and J.-W. Pan, *Science* **354**, 83 (2016).

[56] B. Song, L. Zhang, C. He, T. F. J. Poon, E. Hajiyev, S. Zhang, X.-J. Liu, and G.-B. Jo, *Sci. Adv.* **4**, eaao4748 (2018).

[57] Y. Wang, L. Zhang, S. Niu, D. Yu, and X.-J. Liu, *Phys. Rev. Lett.* **125**, 073204 (2020).

[58] N. Goldman, G. Juzeliūnas, P. Öhberg, and I. B. Spielman, *Rep. Prog. Phys.* **77**, 126401 (2014).

[59] D.-W. Zhang, Y.-Q. Zhu, Y. X. Zhao, H. Yan, and S.-L. Zhu, *Adv. Phys.* **67**, 253 (2018).

[60] N. R. Cooper, J. Dalibard, and I. B. Spielman, *Rev. Mod. Phys.* **91**, 015005 (2019).

[61] P. Weinberg and M. Bükov, *SciPost Phys.* **7**, 97 (2019).

[62] S. R. White, *Phys. Rev. Lett.* **69**, 2863 (1992).

[63] U. Schollwöck, *Ann. Phys. (N. Y.)* **326**, 96 (2011).

[64] E. P. L. van Nieuwenburg, Y.-H. Liu, and S. D. Huber, *Nature Physics* **13**, 435 (2017).

[65] J. F. Rodriguez-Nieva and M. S. Scheurer, *Nature Physics* **15**, 790 (2019).

[66] K. Kottmann, P. Huembeli, M. Lewenstein, and A. Acín, *Phys. Rev. Lett.* **125**, 170603 (2020).

[67] N. Käming, A. Dawid, K. Kottmann, M. Lewenstein, K. Sengstock, A. Dauphin, and C. Weitenberg, *arXiv preprint arXiv:2101.05712* (2021).

[68] See Supplemental Material for more details.

[69] X. Chen, Z.-C. Gu, Z.-X. Liu, and X.-G. Wen, *Science* **338**, 1604 (2012).

[70] C. Wang, A. C. Potter, and T. Senthil, *Science* **343**, 629 (2014).

[71] T. Morimoto, A. Furusaki, and C. Mudry, *Phys. Rev. B* **92**, 125104 (2015).

[72] D. Xiao, M.-C. Chang, and Q. Niu, *Rev. Mod. Phys.* **82**, 1959 (2010).

[73] H. Pichler, G. Zhu, A. Seif, P. Zoller, and M. Hafezi, *Phys. Rev. X* **6**, 041033 (2016).

[74] D. J. Thouless, M. Kohmoto, M. P. Nightingale, and M. den Nijs, *Phys. Rev. Lett.* **49**, 405 (1982).

[75] S. de Léséleuc, V. Lienhard, P. Scholl, D. Barredo, S. Weber, N. Lang, H. P. Büchler, T. Lahaye, and A. Browaeys, *arXiv:1810.13286v1*.

[76] M. Atala, M. Aidelsburger, J. T. Barreiro, D. Abanin, T. Kitagawa, E. Demler, and I. Bloch, *Nat. Phys.* **9**, 795 (2013).

[77] M. Lohse, C. Schweizer, O. Zilberberg, M. Aidelsburger, and I. Bloch, *Nat. Phys.* **12**, 350 (2015).

[78] S. Nakajima, T. Tomita, S. Taie, T. Ichinose, H. Ozawa, L. Wang, M. Troyer, and Y. Takahashi, *Nat. Phys.* **12**, 296 (2016).

[79] H.-I. Lu, M. Schemmer, L. M. Aycock, D. Genkina, S. Sugawa, and I. B. Spielman, *Phys. Rev. Lett.* **116**, 200402 (2016).

[80] C. Schweizer, M. Lohse, R. Citro, and I. Bloch, *Phys. Rev. Lett.* **117**, 170405 (2016).

[81] S. Nakajima, N. Takei, K. Sakuma, Y. Kuno, P. Marra, and Y. Takahashi, *arXiv:2007.06817v1*.

[82] Y. Kuno and Y. Hatsugai, *Phys. Rev. Research* **2**, 042024 (2020).

[83] K. Li, J.-H. Wang, Y.-B. Yang, and Y. Xu, *2104.14097v1*.

**Supplemental Materials for
Connecting Topological Anderson and Mott Insulators in Disordered Interacting Fermionic Systems**

A. Finite-size scaling and ground state degeneracy

In this section, we present finite-size scalings of the topological invariant and excitation gap, and give the numerical evidence of the ground state degeneracy in the topological regions. We first show the Berry phase γ calculated in our DMRG simulation up to $L = 48$ sites, and establish this quantized topological invariant can preserve in the large- L limit by extrapolation. In Fig. 5(a), the finite-size scaling of the Berry phase γ is plotted as a function of $1/L$ in the topological ($W/t = 2.2$) and trivial ($W/t = 1.8$) regions near the phase transition boundary. The twist phase interval $[0, 2\pi]$ is equally cut into 24 parts, the offset phase is fixed to $\varphi = 0$. We have checked the convergence of the Berry phase with the twist phase interval cut into 40 parts. In each DMRG simulation, we keep up to 600 Schmidt values and use a convergence criterion $|\Delta E_g|/E_g < 10^{-8}$ of the ground state (and the first excited state if calculated). These criteria are also used in other DMRG simulations involved in this work. We further calculate the excitation gap in topological phases (TMI, DCTI, and TAI) under PBC and do the finite-size scaling to see whether the gap can preserve in the thermodynamic limit. Figure 5 (b) shows the excitation gap scalings of four typical parameters in the topological region, and the linear fits indicate that Δ_g has finite value when $L \rightarrow \infty$.

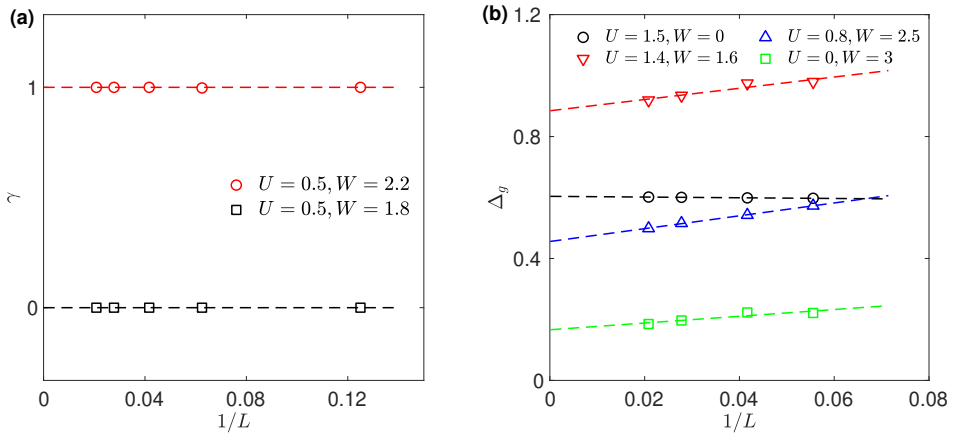


FIG. 5. (Color online) Finite-size scalings of the topological invariant γ (a) and excitation gap Δ_g (b). The parameters are $t = 1$, $t_s = 0.95$, $m_z = 3$, $\alpha = (\sqrt{5} - 1)/2$, and offset phase $\varphi = 0$ for (a) and 20 offset phases are averaged for (b). Dashed lines are linear fits of the numerical data.

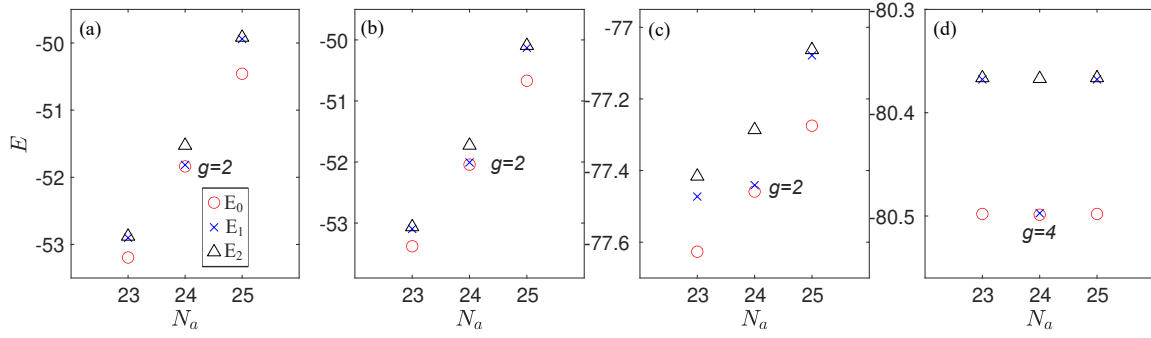


FIG. 6. (Color online) Energies E of lowest three states near the half filling under OBC with total atomic numbers $N_a = L - 1, L, L + 1$ for the TMI with $U = 1.5$ and $W = 0$ (a), the DCTI with $U = 1.5$ and $W = 0.5$ (b), the DCTI with $U = 0.2$ and $W = 3$ (c), and the TAI with $U = 0$ and $W = 3$ (d). Parameters are $t = 1$, $t_s = 0.95$, $m_z = 3$, $\alpha = (\sqrt{5} - 1)/2$, $L = 24$, and 20 different offset phases are averaged when $W \neq 0$.

We further present the degenerate ground state energies of the topological phases under OBC. In the trivial regions, we obtain the single ground state without degeneracy ($g = 1$ and not shown here). For the topological phases of

noninteracting ($U = 0$ for the TAI) and interacting ($U \neq 0$ for the TMI and the DCTI) fermions, the ground state are fourfold and twofold degenerate with $g = 4$ and $g = 2$, respectively. In Fig. 6, we plot the lowest three eigenenergies near the half filling with the particle numbers $N_a = L - 1, L, L + 1$ with the system size $L = 24$ for four typical cases. The interacting cases are simulated from the DMRG while the noninteracting case is calculated from the single-particle representation. In Fig. 6(d) for the noninteracting TAI, the fourfold ground state degeneracy can be clearly observed as the two zero-energy edge modes can be either empty or occupied. When the interaction is turned on, the ground state degeneracy between twofold as only one topological edge excitation occupied on each edge in this case. As shown in Figs. 6(a-c), the twofold degenerate energy for the ground state of the TMI and DCTI at half filling ($N_a = 24$) is higher (lower) than the ground state energy at filling number $N_a = 23$ ($N_a = 25$).

B. Machine learning the phase diagram in a unsupervised and automated fashion

Recently, machine learning methods are emerging as a versatile toolbox to explore the quantum phase diagrams [64–67]. Especially, the unsupervised learning with anomaly detection has showcased its exceptional applicability in both theory [66] and experiments [67]. In this part, we apply the unsupervised learning and anomaly detection proposed in Ref. [66] to benchmark the ground-state phase diagram of our model.

We apply the deep neural network autoencoder for anomaly detection. An autoencoder is a type of neural network that consists of two parts as shown in Fig. 7(a). The encoder part takes the high dimensional input x data and maps it to a low latent variable z via a parametrized function $z = f_{\theta_E}(x)$. The decoder part takes the latent variable z and maps it back to $\hat{x} = g_{\theta_D}(z)$. The goal of the autoencoder is to find an efficient representation of the input data x through the encoder at the bottleneck, from which the decoder can reproduce the input data \hat{x} . The parameters θ_E and θ_D are trained via the minimization of the mean squared error loss function $L(x, \hat{x}) = \sum_i |x_i - \hat{x}_i|^2$.

The main idea of anomaly detection scheme is that after training the autoencoder in a region of the phase diagram, it learns the characteristic features of the phase where the data were taken from and fails to reproduce data from the other phases. Therefore, the failure leads to a higher loss, from which we deduce that the data do not belong to the same phase as the ones used to train the autoencoder. By looking at the loss for all data after training in only part of the phase diagram, we are able to distinguish different phases via different plateaus of the loss function. Furthermore, by fitting the loss curve and finding the transition points, we obtain phase boundaries. Below we use this method based on the autoencoder to benchmark the phase diagram of the model shown in Fig. 1(b).

In order to explore the topological properties of model, we use entanglement spectrum [64] as our input data x to explore the phase diagram of our model. We note that half-chain entanglement has already indicated the regimes for the topologically trivial and the nontrivial phases as shown in Figs. 2(b). The entanglement spectrum also plays an important role in the characterization of many-body quantum systems and is experimentally accessible in cold atom systems [73]. We divide the whole system into two equal subsets A and B , after which the reduced density matrix of subset A is calculated by partially tracing out the degrees of freedom in B : $\rho_A = \text{Tr}_B |\psi^g\rangle\langle\psi^g|$. Denoting the eigenvalues of ρ_A as λ_i , the entanglement spectrum is defined as the set of numbers $-\ln \lambda_i$. The input data are 32×8 matrices, each row of which consist of the largest 8 eigenvalues λ_i for 32 different twist boundary phases θ s. Here the autoencoder is a convolutional neural network and the encoder part consists of two convolution layers, which have 16 kernels of size 2×2 with 2 strides, 8 kernels of size 2×2 with 2 strides, respectively. Following the decoder part are two upsampling convolutional layers both have 16 kernels of size 2×2 with 2 strides. Finally, a convolutional layer with 1 kernel of size 2×2 is used to reproduce the output with the same dimension as the input.

Assuming no a prior knowledge, we start by training data points at the parameter space $(U/t, W/t) \in [0, 0.5] \times [0, 1]$, which is the ordered trivial BI phase according to Fig. 2(a). By testing with data points from the whole phase diagram, we can clearly distinguish the boundaries between the trivial phase and the non-trivial phase in Fig. 7(b). The different loss levels and the sharp transitions at the phase boundaries indicate two different phases.

We also use another experimentally accessible quantity, i.e., the local spin density $\langle n_{j\sigma} \rangle$ to reveal the phase transitions from the trivial BI to the topological phases. The input data of the local spin density are $2L \times 1$ matrices of the form $[\langle n_{1\uparrow} \rangle, \langle n_{1\downarrow} \rangle, \langle n_{2\uparrow} \rangle, \langle n_{2\downarrow} \rangle, \dots, \langle n_{L\uparrow} \rangle, \langle n_{L\downarrow} \rangle]$. We numerically generate the data for each pair of parameters over 20 quasiperiodic configurations with respect to the offset phase φ . Now the autoencoder is taken as a fully connected neural network consisting of three hidden layers which have 8, 4 and 8 neurons, respectively. We take the training data points at the parameter space $(U/t, W/t) \in [0, 0.5] \times [0, 1]$, which is the ordered trivial BI. After training, we can obtain the boundaries between the trivial BI to the topological phases. Overall, the phase boundaries predicted by this unsupervised and automated machine learning match well with those obtained from the ED and DMRG simulations.

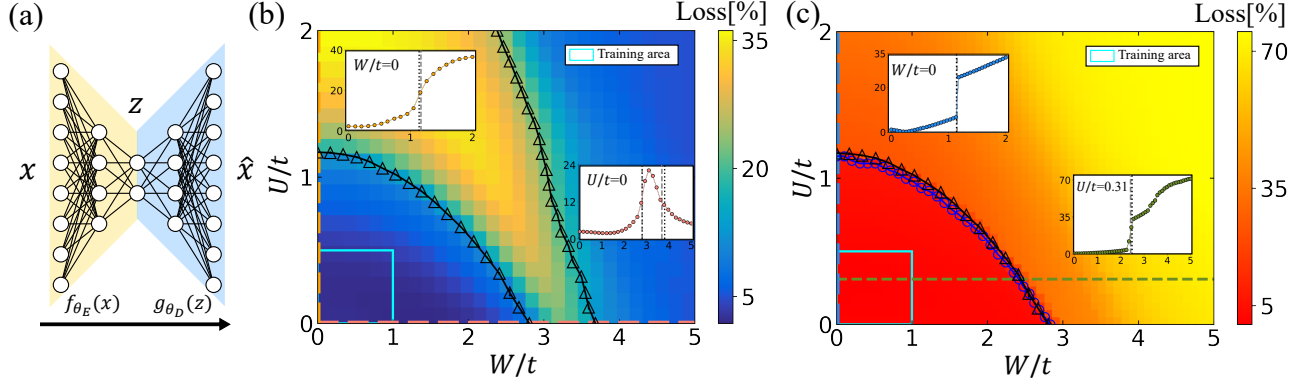


FIG. 7. (Color online) (a) Schematic of the autoencoder with encoder and decoder. The input data x are mapped to the low bottleneck z via encoder $z = f_{\theta_E}(x)$ and decoded to $\hat{x} = g_{\theta_D}(z)$. (b) 2D loss map of the autoencoder after training at the parameter space $(U/t, W/t) \in [0, 0.5] \times [0, 1]$ (blue square frame). The insets show the loss along the dashed lines. Vertical gray dashed (black dotted) lines in the insets are the transitions obtained by the anomaly detection (the ED and DMRG simulations). Two different phases are distinguished via different plateaus of loss value. The black triangle guided by the solid line denotes the topological phase boundaries determined by using anomaly detection. (c) 2D loss map of the autoencoder after training at the parameter space $(U/t, W/t) \in [0, 0.5] \times [0, 1]$ (blue square frame). The insets show the loss along the dashed lines. Vertical gray dashed (black dotted) lines in the insets are the transitions obtained by the anomaly detection (the ED and DMRG simulations). Two different phases are distinguished via different plateaus of loss value. The blue circle symbols guided by solid line denotes the boundaries between the trivial BI to the topological phases. The black triangle guided by the solid line are the same line in the (b).

C. Mean field and self-consistent Born approximations

In this part, we describe some details of the unified analysis of the topological phase transitions from the trivial BI driven by the disorder and interaction. The density-density interaction term can be linearized by the Hartree-Fock MF approximation [46]

$$n_{j\sigma}n_{j+1\sigma} \approx \langle n_{j\sigma} \rangle n_{j+1\sigma} + \langle n_{j+1\sigma} \rangle n_{j\sigma} - \langle n_{j\sigma} \rangle \langle n_{j+1\sigma} \rangle. \quad (3)$$

In the trivial BI phase, the fermion density of each spin component of the ground state is approximately site-independent, and the Hartree-Fock MF approximation can be simplified to

$$U \sum_{j=1}^L n_{j\sigma} n_{j+1\sigma} \approx \frac{2N_\sigma U}{L} \sum_{j=1}^L n_{j\sigma} + \text{const.}, \quad (4)$$

where N_σ is the total occupation of spin- σ fermions. We plot the density distributions of fermions calculated from both ED method and Hartree-Fock MF approach in Fig. 8(a), which shows that the spin density is indeed site-independent and the MF ground state fairly captures the exact ground state property even near the trivial BI phase boundary ($U/t = 1$). In this case, the density difference between spins $\langle n_\uparrow \rangle < \langle n_\downarrow \rangle$. By defining the density difference $\rho_s \equiv (N_\downarrow - N_\uparrow)/L > 0$, the interaction term under the MF approximation can be further expressed as

$$\sum_{\sigma=\{\uparrow, \downarrow\}} \frac{2N_\sigma U}{L} \sum_{j=1}^L n_{j\sigma} = \sum_{j=1}^L [-\rho_s U (n_{j\uparrow} - n_{j\downarrow}) + U (n_{j\uparrow} + n_{j\downarrow})] = U N_a - \rho_s U \sum_{j=1}^L (n_{j\uparrow} - n_{j\downarrow}), \quad (5)$$

where ρ_s affects the σ_z component of the model and the interaction U can renormalize the Zeeman strength as [46]

$$\tilde{m}_z = m_z - \rho_s U, \quad (6)$$

up to an irrelevant constant energy UN_a . As is shown in Fig. 8(a), we numerically determine $\rho_s \approx 1/1.14$. We apply Eq. (6) to accurately characterize the phase boundary of the trivial BI and TMI in the clean limit.

As is discussed in the main text, the fidelity \mathcal{F} of the ground state against disorder reveals that the trivial BI phase is ordered, and the above MF approach can be fairly applied. We further consider the MF relation in Eq. (6) with nonzero disorder W and include the neighboring density-density interaction U into the Zeeman strength m_z to

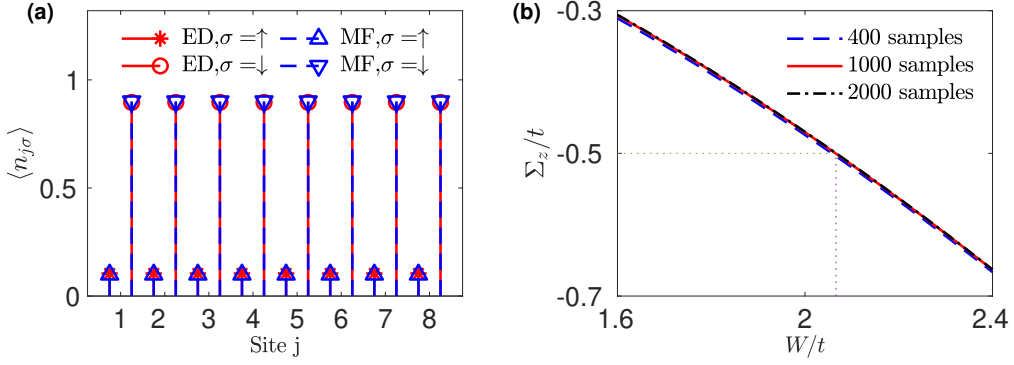


FIG. 8. (Color online) (a) Density distribution of each spin component for ED and MF approximated ground states in the clean limit. Parameters are chosen as $t = 1$, $t_s = 0.95$, $m_z = 3$, $U = 1$, and $L = 8$. (b) The self-energy parameter Σ_z as a function of W for results averaged from 400, 1000, 2000 number of disorder samples. Dotted lines indicate the critical disorder W_c for $\tilde{m}_z + \Sigma_z = 2t$. Parameters are $t = 1$, $t_s = 0.95$, $m_z = 3$, $U = 0.57$, $\alpha = (\sqrt{5} - 1)/2$, and $\varphi = 0$.

analysis the topological phase boundary. The effects of disorder can be accounted as the self-energy from the effective medium theory and SCBA under as [6–8]

$$\begin{aligned} \frac{1}{E_f - H_{\text{MF}}(k) - \Sigma(W)} &= \langle \frac{1}{E_f - H_{\text{eff}}(k, W_q)} \rangle_q, \\ H_{\text{MF}}(k) &= [\tilde{m}_z - 2t \cos(k)]\sigma_z - 2t_s \sin(k)\sigma_y, \\ H_{\text{eff}}(k, W_q) &= [\tilde{m}_z - 2t \cos(k) + W_q]\sigma_z - 2t_s \sin(k)\sigma_y, \end{aligned} \quad (7)$$

where E_f is the Fermi energy and is set to zero in our model, $\sigma_{y,z}$ are Pauli matrices, $H_{\text{MF}}(k)$ is the clean Hamiltonian under MF approximation, $\Sigma(W)$ is the self energy under the specify disorder strength W , $H_{\text{eff}}(k, W_q)$ is the effective two-band disordered Hamiltonian with random parameter $W_q = W \cos(2\pi\alpha q)$ denoted by the index $q = 1, 2, \dots, N_q$, and $\langle \dots \rangle_q$ denotes averaging over N_q disorder configurations.

Our numerical result indicates the self-energy has form $\Sigma = \Sigma_z \sigma_z + \Sigma_y \sigma_y$, with the z component effectively renormalizes the Zeeman term $\tilde{m}_z \rightarrow \tilde{m}_z + \Sigma_z$, and the y component renormalizes the hopping parameter $t_s \rightarrow t_s + \Sigma_y$ which is irrelevant to the topological phase transition. In Fig. 8(b), we extract and plot Σ_z as a function of the disorder strength W , which are averaged over different momenta k and different sample numbers $N_q = 400, 1000, 2000$. We find that Σ_z tends to small value with increasing W , and the critical value W_c is determined by the renormalized topological phase boundary $\tilde{m}_z + \Sigma_z = 2t$ (e.g., $\tilde{m}_z = 2.5$ for $U = 0.57$). In practice, the self-energy converges quickly when increasing N_q and we use $N_q = 1000$ disorder samples in the main text.

D. Discontinuous change of total magnetization at the topological phase transition

Here we numerically study the total magnetization \mathcal{M} as a local order parameter to provide the first-order character of the quantum phase transition from the trivial BI to the topological phases. The total magnetization \mathcal{M} in this spin-1/2 system is defined as

$$\mathcal{M} = \frac{1}{L} \sum_{j=1}^L \langle \psi^g | n_{j\uparrow} - n_{j\downarrow} | \psi^g \rangle, \quad (8)$$

where $|\psi^g\rangle$ is the many-body ground state. In Fig. 9(a), we plot \mathcal{M} as a function of W and U , which is obtained from the ED and averaged over 20 random samples. The result shows a discontinuous change near the phase boundary (determined by other quantities as discussed in the main text) between trivial BI and the topological phases. To see the discontinuous change of \mathcal{M} with respect to W or U more clearly, we further calculate the corresponding first derivatives $\delta\mathcal{M}(x)/\delta x$ with $x = U, W$. Numerically, the first derivative $\delta\mathcal{M}(x)/\delta x$ at $x = x_0$ up to the second order approximation is given by

$$\frac{\delta\mathcal{M}(x)}{\delta x} \Big|_{x=x_0} \approx \frac{-\mathcal{M}(x_0 + 2\delta x) + 8\mathcal{M}(x_0 + \delta x) - 8\mathcal{M}(x_0 - \delta x) + \mathcal{M}(x_0 - 2\delta x)}{12\delta x}, \quad (9)$$

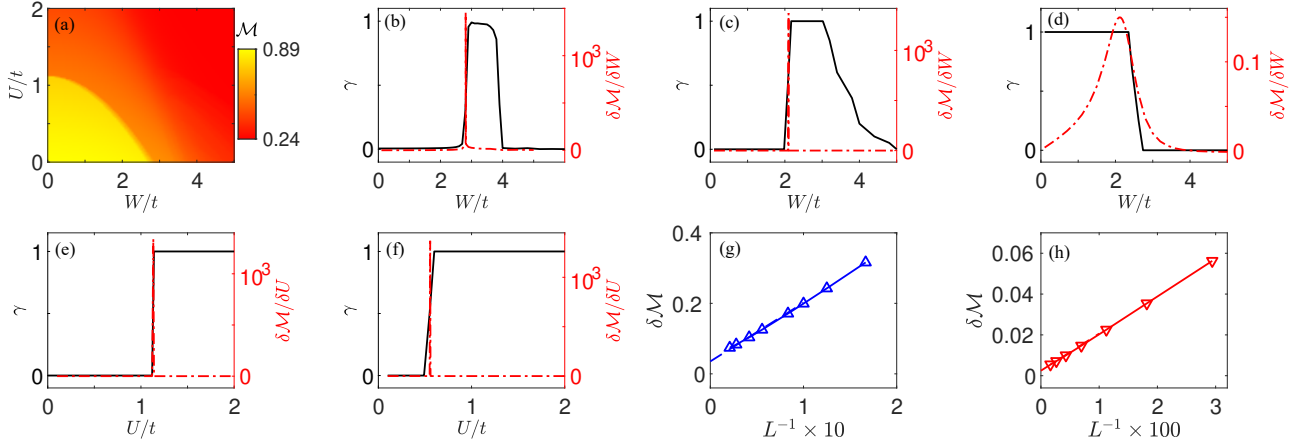


FIG. 9. (Color online) (a) The total magnetization \mathcal{M} as a function of U and W for $L = N_a = 8$ systems. A minus sign is added to \mathcal{M} because $\mathcal{M} < 0$ in our model. (b-f) The first derivative of \mathcal{M} along with the Berry phase plotted as functions of U or W for $U = 0$ (b), $U = 0.5$ (c), $U = 2.0$ (d), $W = 0$ (e), $W = 2$ (f); $L = 610$ for $U = 0$ and $L = 8$ for other parameters. (g,h) The finite-size scaling of the magnetization change $\delta\mathcal{M}$ near the phase transition point as functions of inverse system size $1/L$ for interaction-induced (g) and disorder-induced (h) phase transitions at $W = 0$ and $U = 0$, respectively. Other parameters are $t = 1$, $t_s = 0.95$, $m_z = 3$, and $\alpha = (\sqrt{5} - 1)/2$.

and $\delta x = 10^{-4}$ is chosen in the numerical calculation. In Figs. 9(b-f), we plot the first derivative $\delta\mathcal{M}/\delta x$ as functions of U or W for five typical situations discussed in the main text. The interaction or disorder induced topological phase transitions from the trivial BI to the DCTI are accompanied by the divergence of $\delta\mathcal{M}/\delta x$ near the transition points. This indicates the disorder/interaction induced topological phase transitions have the character of first order phase transitions with discontinuous change of the total magnetization as a local order parameter. However, the transitions from the topological phases to the disordered trivial phase induced by stronger disorders shows no divergence of $\delta\mathcal{M}/\delta W$ [see Fig. 9(d)].

To confirm that the discontinuity of the total magnetization can survive in the large L limit, we perform the finite-size scaling of the magnetization change $\delta\mathcal{M} \equiv \mathcal{M}(x_c + \delta x) - \mathcal{M}(x_c - \delta x)$, which denotes the difference of the total magnet \mathcal{M} between the right and left sides of the phase transition point x_c (with the $\delta x = 10^{-4}$). We present numerical results for the clean limit and the non-interacting limit in Figs. 9(g) and 9(h), respectively. The extrapolations of $\delta\mathcal{M}$ to the $1/L \rightarrow 0$ limit indicate the discontinuous magnetization change can exist in the large L limit. Thus, we argue that the first-order topological quantum phase transition induced by the disorder/interaction preserves in the thermodynamic limit.

E. Results for the case of $m_z = 4$ and the random disorder case

We present numerical results of the quantized Berry phase γ as functions of W and U for $m_z = 4$ in Fig. 10(a), in which case the DCTI phase induced by the combination of disorder and interaction remains while the noninteracting TAI phase is absent. The phase transitions from the trivial BI to the topological phases accompany with the gap closing as shown in Fig. 10(b). The half-chain entanglement \mathcal{S} and the ground-state fidelity \mathcal{F} (against disorder) are plotted in Figs. 10(c) and 10(d), respectively. The large entanglement signals the topological states are highly entangled and the fidelity suggests that trivial BI phase is ordered and the others are disordered. These numerical results consist with those for $m_z = 3$, except the absence of disorder-induced TAIs in the noninteracting limit for $m_z = 4$.

We also consider the random disorder by replacing the quasiperiodic disorder $m_j = m_z + W \cos(2\pi\alpha j + \varphi)$ with the random disorder $m_j = m_z + W_j$ in the model Hamiltonian (1) in the main text, where W_j is uniformly distributed in $[-W, W]$. We display the Berry phase γ on the $W-U$ plane for $L = N_a = 8$ and $m_z/t = 2.4$ in the random disorder case, as shown in Fig. 11(a). Although γ is not well quantized near the phase boundary due to the finite size and fluctuation effects in this case, the disorder and interaction induced topological phase transitions from the trivial BI to the DCTI can also be observed. The red dashed curve is the phase boundary obtained from the MF and SCBA approaches. In Fig. 11(b), the excitation gap Δ_g is displayed for a certain random disorder configuration, which clearly shows the gap closing near the topological phase transition from the BI to topological phases. To reduce the

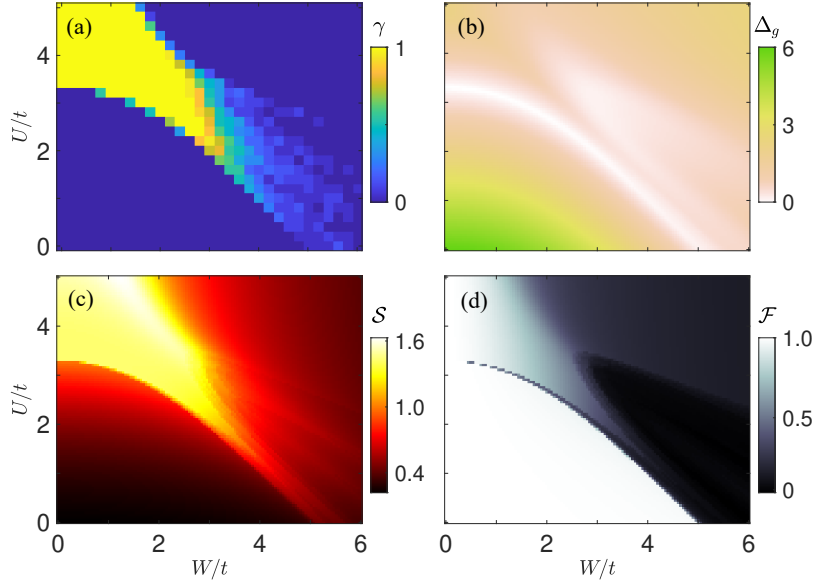


FIG. 10. (Color online) (a) Berry phase γ , (b) excitation gap Δ_g , (c) half-chain entanglement S , and (d) ground-state fidelity \mathcal{F} plotted as functions of W or U for $m_z = 4$. Other parameters are the same to Fig. 1 in the main text.

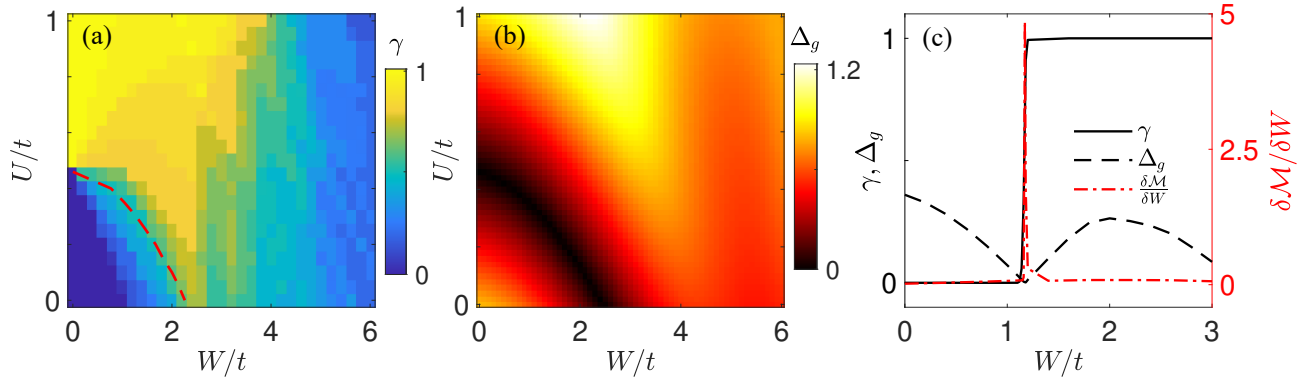


FIG. 11. (Color online) (a) Berry phase γ and (b) excitation gap Δ_g on the W - U plane for $m_z = 2.4$ and $L = N_a = 8$ obtained from the ED. The red dashed curve is the phase boundary obtained from the MF and SCBA approaches. The data in (a) are averaged over 20 random disorder realizations. (c) Berry phase γ , excitation gap Δ_g , and first derivative of \mathcal{M} as a function of W for a disorder configuration with $U = 0.25$, $m_z = 2.4$ and $L = 24$ obtained from the DMRG. Other parameters are $t = 1$ and $t_s = 0.95$.

finite size effect of the random disorder, we further plot the DMRG result for a larger system with $L = N_a = 24$ in Fig. 11(c), where the Berry phase γ , excitation gap Δ_g , and the first derivative of the total magnetization $\delta\mathcal{M}/\delta W$ as a function of W are plotted. The Berry phase γ is now well quantized in the DMRG simulation, and the results show the topological phase transition accompanied by the gap closing and the divergence of the first derivative of the total magnetization. These results are similar to those for the quasiperiodic disorder discussed in the main text. This indicates that the adiabatical connection between the TAI and TMI phases, the DCTI phase, and the unified analysis of the topological phase transitions in the main text preserve for both quasiperiodic and random disorders.